Phase Behavior of Electrostatically Complexed Polyelectrolyte Gels Using an Embedded Fluctuation Model

Debra J. Audus[a,b,‡], Jeffrey D. Gopez[a,b], Daniel V. Krogstad[a,c,x], Nathaniel A. Lynd[a,¶], Edward J. Kramer[a,b,c], Craig J. Hawker[a,c,d], Glenn H. Fredrickson[*a,b,c]

1 Eigen decomposition

The Eigen decomposition used in Sec. 2.1 is a mathematically exact transformation that allows for the use of the Hubbard-Stratonovich transformation without the introduction of explicit density fields. Essentially, it is a method for making the interactions, in this case, excluded volume interactions, quadratic. The relevant potential energy is

$$\beta U_{exv} = \frac{1}{2}\int d\mathbf{r}\, P(\mathbf{r})^T \mathbf{B} P(\mathbf{r}) \tag{1}$$

where

$$\mathbf{B} = \begin{pmatrix} B_{ee} & B_{em} \\ B_{em} & B_{mm} \end{pmatrix}, \tag{2}$$

$$P(\mathbf{r}) = \begin{pmatrix} \hat{\rho}_{e+}(\mathbf{r}) + \hat{\rho}_{e-}(\mathbf{r}) \\ \hat{\rho}_{m+}(\mathbf{r}) + \hat{\rho}_{m-}(\mathbf{r}) \end{pmatrix}. \tag{3}$$

Since $\mathbf{B}$ is purely real and symmetric,

$$\mathbf{B} = \mathbf{U}\mathbf{D}\mathbf{U}^T \tag{4}$$

where

$$\mathbf{D} = \begin{pmatrix} d_1 & 0 \\ 0 & d_2 \end{pmatrix}, \tag{5}$$

$$\mathbf{U} = \begin{pmatrix} U_{11} & U_{12} \\ U_{21} & U_{22} \end{pmatrix}. \tag{6}$$

$(U_{ij}\, U_{2j})$ is the normalized eigenvector and d_j is the corresponding eigenvalue from the Eigen decomposition of $\mathbf{B}$. Consequently, Eq. 1 can now be simplified.

$$\beta U_{exv} = \frac{1}{2}\int d\mathbf{r}\, P(\mathbf{r})^T \mathbf{U}\mathbf{D}\mathbf{U}^T P(\mathbf{r}) \tag{7}$$

$$= \frac{1}{2}\int d\mathbf{r}\, (\mathbf{U}^T P(\mathbf{r}))^T \mathbf{D} (\mathbf{U}^T P(\mathbf{r})) \tag{8}$$

$$= \sum_{j=1}^{2} \int d\mathbf{r}\, d_j (U_{1j}(\hat{\rho}_{e+} + \hat{\rho}_{e-}) + U_{2j}(\hat{\rho}_{m+} + \hat{\rho}_{m-}))^2 \tag{9}$$

[0a] *Materials Research Laboratory, University of California, Santa Barbara, USA*
[0b] *Department of Chemical Engineering, University of California, Santa Barbara, USA*
[0c] *Materials Department, University of California, Santa Barbara, USA*
[0d] *Department of Chemistry and Biochemistry, University of California, Santa Barbara, USA*
[0‡] Present address: National Institute of Standards and Technology
[0§] Present address: Illinois Applied Research Institute
[0¶] Present address: Lawrence Berkeley National Laboratory

Since there are no approximations, Eq. 9 is equal to Eq. 1. However, Eq. 9 can now be used for direct Hubbard-Stratonovich transformations of each term in the sum, since it is quadratic in a linear combination of the density fields. If one of the eigenvalues is zero, no Hubbard-Stratonovich is performed for that term in the sum, since it has no contribution to U_{exv}.

2 Simplification of the model with embedded electrostatic fluctuations

The form of the electrostatic contribution to the potential energy in the model with embedded electrostatic fluctuations has two independent parameters and requires numerical integration.

$$\beta U_{el} = \frac{1}{4\pi^2} \int d\mathbf{r} \int_0^\infty dk\, k^2 \ln\left(1 + (\hat{\rho}_{e+}(\mathbf{r}) + \hat{\rho}_{e-}(\mathbf{r}))\frac{E\hat{g}_{D,e}(f,k^2)\hat{\Gamma}^2(k^2)}{fk^2}\right) \tag{10}$$

To avoid these complications, we made the following replacement

$$\frac{1}{f}\hat{g}_{D,e}(k^2,f) \approx \hat{g}_D(k^2,1), \tag{11}$$

which eliminates the direct dependence on f. Both functions have the same high k limit, and this substitution provides reasonable quantitative agreement when comparing phase behavior. To illustrate this point, see Fig. 1 where the phase diagram considering only macrophase separation is shown both with and without this approximation.

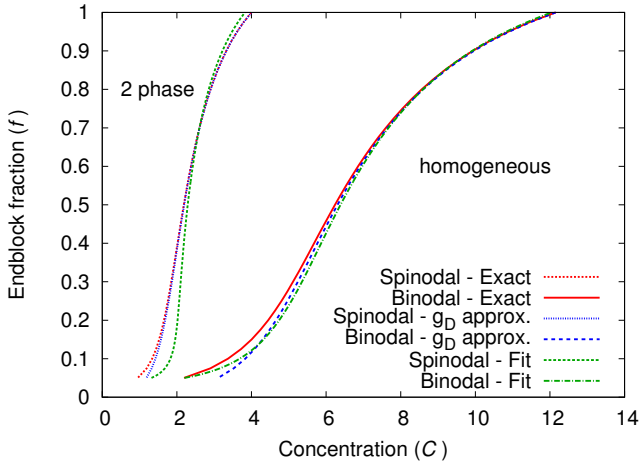

Figure 1: Comparison of the original one-loop phase diagram, the phase diagram with the Debye function substitution and the phase diagram generated using a fitting procedure for parameters of $E = 500,000, B_{ee} = 1, B_{em} = B_{mm} = 3$.

Then, to avoid numerical integration, we made the following approximation

$$\beta U_{el} = \int d\mathbf{r}\, h[(\hat{\rho}_{e+}(\mathbf{r}) + \hat{\rho}_{e-}(\mathbf{r}))E] \tag{12}$$

where

$$h(xE) = \frac{\xi xE}{(1+\kappa xE)^\gamma}, \tag{13}$$

and ξ, κ and γ are fitting parameters. This particular functional form was chosen for two reasons. First, it is a good approximation for $(\hat{\rho}_{e+}(\mathbf{r}) + \hat{\rho}_{e-}(\mathbf{r}))E$ between 1e5 and 5e7, which corresponds to $(\hat{\rho}_{e+}(\mathbf{r}) + \hat{\rho}_{e-}(\mathbf{r}))$ between 0.2 and 100 for an E of 500,000. Second, when xE, or equivalently $(\hat{\rho}_{e+}(\mathbf{r}) + \hat{\rho}_{e-}(\mathbf{r}))E$, is small,

$$h(xE) \approx \xi xE \tag{14}$$

which means that the maximum electrostatic contribution to ψ, ξE, can be set explicitly with a choice of ξ. This requirement is critical because if we fit the one-loop functional form exactly, the maximum electrostatic contribution to ψ would be $8.76E$, which for a reasonable E of 500,000 would result in a maximum electrostatic contribution to ψ of 4.4e6. ψ values this large would introduce both stability issues and error into the SCFT simulations. Instead, we chose to limit the maximum electrostatic contribution to ψ at a much more reasonable value of $(7.6\text{e-}4)E$ (or $\exp(-3.5)E/(4\pi^2)$), which corresponds to 380 for $E = 500,000$. These choices mean that the low densities will not be simulated accurately; however, for practical purposes it does not matter if the regions of low density have their expected value of 1e-40 or their predicted value of 1e-8. When viewing density profiles, both values appear to be essentially zero. Additionally, properties of interest are unaffected.

After performing the fit, we find $\kappa = 2.5\text{e-}5$ and $\gamma = 0.731$. As can be seen in Fig. 2, for the region of interest there is good agreement between the fit and the full numerical integral. This fit also yields a phase diagram for macrophase separation that is in good agreement with the one-loop phase diagram as can be seen in Fig. 1.

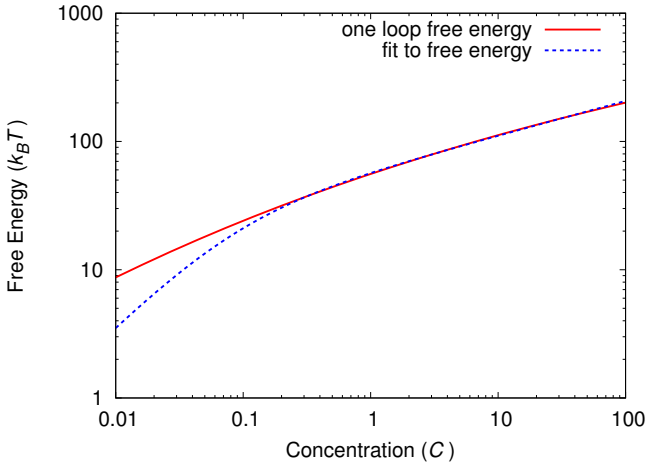

Figure 2: The fit of the electrostatic free energy from the one-loop approximation for $E = 500,000$.

Rather than using steepest descent (or ascent) to find the saddle points for all four fields, which would be computationally expensive, we first compute $\frac{\delta H}{\delta \rho_e}$ and $\frac{\delta H}{\delta \rho_m}$, set these equal to zero, and find

$$\psi(\mathbf{r}) = -i\left(B_{em}\rho_m(\mathbf{r}) + B_{ee}\rho_e(\mathbf{r}) + \left.\frac{\partial h(xE)}{\partial x}\right|_{x=\rho_e(\mathbf{r})}\right), \tag{15}$$

$$w(\mathbf{r}) = -i\left(B_{em}\rho_e(\mathbf{r}) + B_{mm}\rho_m(\mathbf{r})\right). \tag{16}$$

We then plug these quantities back into the Hamiltonian and solve for $\frac{\delta H}{\delta \rho_e}$ and $\frac{\delta H}{\delta \rho_m}$, which yields

$$\frac{\delta H}{\delta \rho_e(\mathbf{r})} = B_{em}(\tilde{\rho}_m(\mathbf{r}) - \rho_m(\mathbf{r})) + \left(B_{ee} + \left.\frac{\partial^2 h(xE)}{\partial x^2}\right|_{x=\rho_e(\mathbf{r})} \right) (\tilde{\rho}_e(\mathbf{r}) - \rho_e(\mathbf{r})) = 0, \tag{17}$$

$$\frac{\delta H}{\delta \rho_m(\mathbf{r})} = B_{mm}(\tilde{\rho}_m(\mathbf{r}) - \rho_m(\mathbf{r})) + B_{em}(\tilde{\rho}_e(\mathbf{r}) - \rho_e(\mathbf{r})) = 0. \tag{18}$$

Notice that both of these equations are satisfied if

$$\Gamma(\mathbf{r}) * \tilde{\rho}_j(\mathbf{r}) - \rho_j(\mathbf{r}) = 0 \tag{19}$$

where $j = e, m$. Therefore, we solve

$$\frac{\partial \rho_j(\mathbf{r}, t)}{\partial t} = -\left(\Gamma(\mathbf{r}) * \tilde{\rho}_j(\mathbf{r}, t) - \rho_j(\mathbf{r}, t)\right) \tag{20}$$

for both of the densities ($j = e, m$) and then calculate the w and ψ fields from Eqs. 16 and 15 in order to find the saddle points for all four fields. This procedure is more direct and less computationally expensive than solving for all four fields with a steepest descent (or ascent).

3 Structure factor

In order to extract extra structural information from the FTS-CL, we used structure factors corresponding to the end-block/end-block correlations.

$$S(k) = \frac{1}{V} \int d\mathbf{r} \int d\mathbf{r}' e^{-i\mathbf{k}\cdot(\mathbf{r}-\mathbf{r}')} \langle (\hat{\rho}_{e+}(\mathbf{r}) + \hat{\rho}_{e-}(\mathbf{r}))(\hat{\rho}_{e+}(\mathbf{r}') + \hat{\rho}_{e-}(\mathbf{r}'))\rangle \tag{21}$$

The end-block/end-block density correlation is found to be

$$\begin{aligned}
&\langle (\hat{\rho}_{e+}(\mathbf{r}) + \hat{\rho}_{e-}(\mathbf{r}))(\hat{\rho}_{e+}(\mathbf{r}') + \hat{\rho}_{e-}(\mathbf{r}'))\rangle = \\
&\quad \sigma^2 N^2 \left(\frac{\mathcal{Z}_0}{\mathcal{Z}_C} \int \mathcal{D}w_1 \int \mathcal{D}w_2 \int \mathcal{D}\psi \, e^{-\sum_{j=1}^{2} \frac{1}{2|d_j|} \int d\mathbf{r}\, w_j(\mathbf{r})^2 + \frac{1}{2E} \int d\mathbf{r}\, \psi(\mathbf{r}) \nabla^2 \psi(\mathbf{r})} \right) \\
&\qquad \left(- e^{n \ln Q[\Gamma * w_+]} \frac{\delta^2 e^{n \ln Q[\Gamma * w_-]}}{\delta\psi(\mathbf{r})\delta\psi(\mathbf{r}')} - e^{n \ln Q[\Gamma * w_-]} \frac{\delta^2 e^{n \ln Q[\Gamma * w_+]}}{\delta\psi(\mathbf{r})\delta\psi(\mathbf{r}')} \right. \\
&\qquad\qquad \left. + \frac{\delta e^{n \ln Q[\Gamma * w_+]}}{\delta\psi(\mathbf{r})} \frac{\delta e^{n \ln Q[\Gamma * w_-]}}{\delta\psi(\mathbf{r}')} + \frac{\delta e^{n \ln Q[\Gamma * w_-]}}{\delta\psi(\mathbf{r})} \frac{\delta e^{n \ln Q[\Gamma * w_+]}}{\delta\psi(\mathbf{r}')} \right)
\end{aligned} \tag{22}$$

Splitting up each of the four terms in parentheses, using functional integration by parts once, and plugging the result in Eq. 21 results in

$$S(\mathbf{k}) = \frac{\sigma^2 N^2}{V} \left(\frac{k^2}{E} \langle i\hat{\psi}(\mathbf{k})(\hat{\tilde{\rho}}_{e+}(-\mathbf{k}) - \hat{\tilde{\rho}}_{e-}(-\mathbf{k})\rangle \right. \tag{23}$$

$$\left. + 2\langle \hat{\tilde{\rho}}_{e+}(\mathbf{k}) \hat{\tilde{\rho}}_{e+}(-\mathbf{k})\rangle + 2\langle \hat{\tilde{\rho}}_{e-}(\mathbf{k}) \hat{\tilde{\rho}}_{e-}(-\mathbf{k})\rangle \right) \tag{24}$$

where $\hat{\tilde{\rho}}$ is the Fourier transform of the density *operator*.

4 Density profiles from FTS-CL

After equilibration of the unit cell simulations of microphases, we computed the average densities. Cross-sections of these average densities can be found in Fig. 4. Note the qualitative agreement with the SCFT simulations cross-sections shown in Fig. 2 of the manuscript.

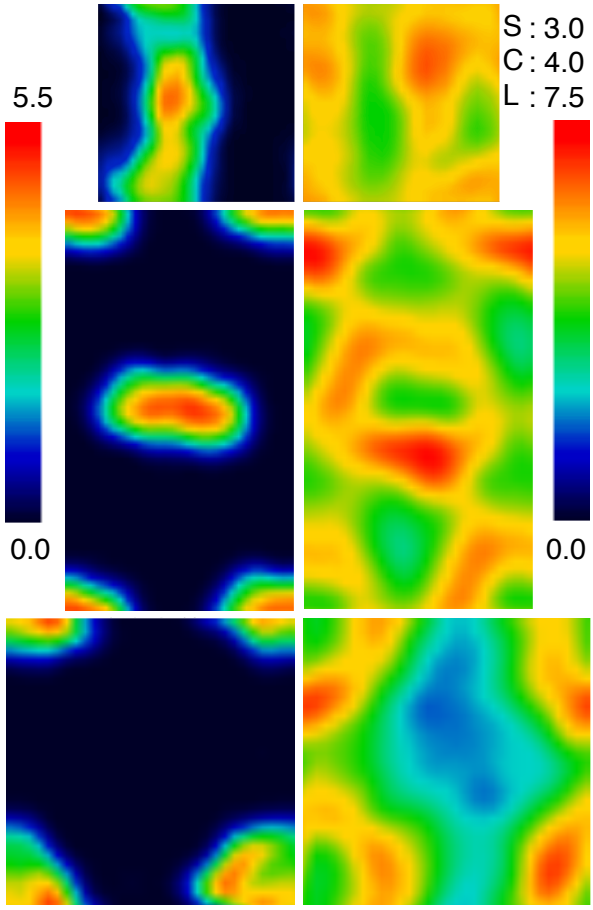

Figure 3: Cross-sections of end-block (left) and mid-block (right) densities of, from top to bottom, lamellae at $C = 6$, hexagonally packed cylinders at $C = 3$, and body-centered cubic spheres at $C = 2$. Parameters are $f = 0.2$, $E = 500,000$, $B_{ee} = 1$ and $B_{em} = B_{mm} = 3$. The mid-block scale bar depends on the structure with L corresponding to lamellae ($C = 6$), C corresponding to hexagonally packed cylinders ($C = 3$) and S corresponding to body-centered cubic spheres ($C = 2$). Images were generated using FTS-CL.

5 Small angle X-ray scattering results

The small angle X-ray scattering (SAXS) results that were used to determine the experimental phase diagram (see Fig. 6 of the manuscript) for an endblock fraction of 0.21 can be found in Fig. 5.

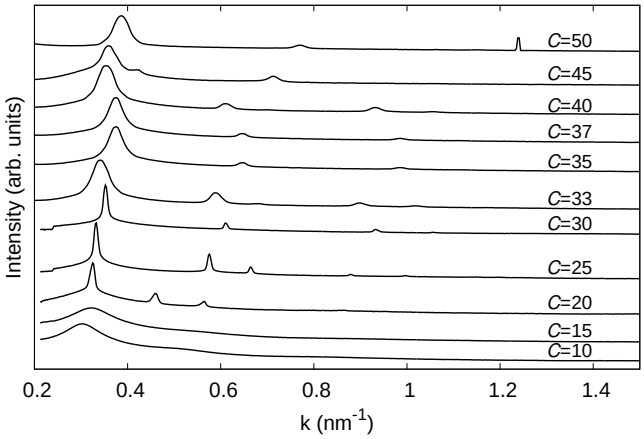

Figure 4: SAXS results for $f = 0.21$ and various C.